ACS Energy LETTERS

http://pubs.acs.org/journal/aelccp

LETTER

Probing the Catalytically Active Region in a Nanoporous Gold Gas Diffusion Electrode for Highly Selective Carbon Dioxide Reduction

Aidan Q. Fenwick,[†] Alex J. Welch,[†] Xueqian Li, Ian Sullivan, Joseph S. DuChene, Chengxiang Xiang, and Harry A. Atwater*

Cite This: *ACS Energy Lett.* 2022, 7, 871−879

Read Online

ACCESS | Metrics & More | Article Recommendations | Supporting Information

ABSTRACT: We report the use of a nanoporous gold (np-Au) catalyst for CO_2 reduction in a gas diffusion electrode (GDE) and characterize the role of wetting in electrochemical performance. The np-Au catalyst has pores on the order of 20 nm and is cross-sectionally isotropic, enabling Faradaic efficiencies for CO of greater than 95% across a wide range of potentials and a maximum partial current density for CO of 168 mA/cm^2. Secondary ion mass spectroscopy and *in situ* copper underpotential deposition were employed to provide insights into catalyst wetting. At a typical CO_2 flow rate of 50 SCCM, approximately half of the catalyst is in contact with the electrolyte during operation, and the dry region exists in the bottom half of the nanoporous catalyst. We discuss implications of the nanoporous GDE wetting characteristics for catalyst performance and the design of improved GDE architectures that can maximize the catalytically active area.

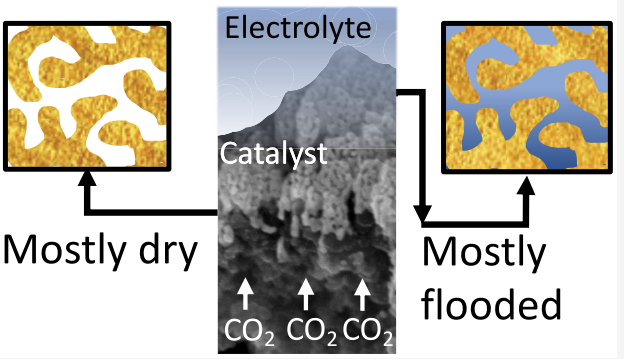

The electrochemical reduction of carbon dioxide to value-added products represents a promising means to store renewable electricity and create a closed carbon cycle for fuels, chemicals, and materials.[1−3] Carbon dioxide reduction (CO_2R) can produce a wide variety of products based on catalyst materials,[4−6] structuring,[4,7] and treatment.[2,8] Of these products, carbon monoxide (CO) is especially interesting due to its ubiquitous role as a precursor in cornerstone chemical processes such as Fischer−Tropsch reactions,[9−11] hydroformylation of alkenes to aldehydes,[12] methanol production,[10,13] and metal refinement.[14] In addition, CO_2R to CO is a two-electron process, which translates to lower energy inputs as compared to other multi-electron products.[10,15] CO production has been demonstrated with high selectivity, with the Faradaic efficiency (FE) for CO reaching >90% in aqueous electrolyzers.[7,8] While current densities between 10 and 20 mA/cm^2 can be achieved through electrode nanostructuring,[16−20] electrochemical CO_2R in bulk aqueous electrolytes is mass transport limited due to low CO_2 solubility and long reactant diffusion lengths.[21,22] In order for electrochemical CO_2R to be economically attractive, current densities greater than 100 mA/cm^2 are thought to be required.[23,24]

Gas diffusion electrodes (GDEs) present an alternative electrode design capable of addressing mass transport limitations.[25] In a GDE, a blend of CO_2 gas and water vapor is flowed across a porous catalyst layer in contact with a liquid electrolyte.[21,25] High current densities have been achieved by GDEs carefully tuned for high performance in a range of different configurations such as alkaline electrolyzers and membrane electrode assemblies.[26−29]

The large disparity in current density observed between an aqueous and GDE-based electrochemical CO_2R cell is mostly attributed to differences in the mass transport limits of CO_2 in these distinct systems. In an aqueous-based electrochemical CO_2R cell, CO_2 must first dissolve into the liquid electrolyte and then diffuse to the electrode surface for the reaction to occur. This process is limited by mass transport due to low CO_2 solubility in the liquid electrolyte, which limits the total

Received: October 17, 2021
Accepted: December 30, 2021
Published: January 27, 2022

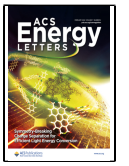

current density on the order of tens of mA/cm^2. In an aqueous electrolyte electrochemical CO_2R cell, the catalyst can be considered completely wet, or flooded, where the catalyst is fully submerged in the electrolyte. On the other hand, an idealized GDE advantageously forms a triple-phase boundary in which a meniscus of electrolyte coats the catalyst ligaments, and vapor channels remain open to permit gas flow through the catalyst layer, as shown in Figure 1. This condition reduces

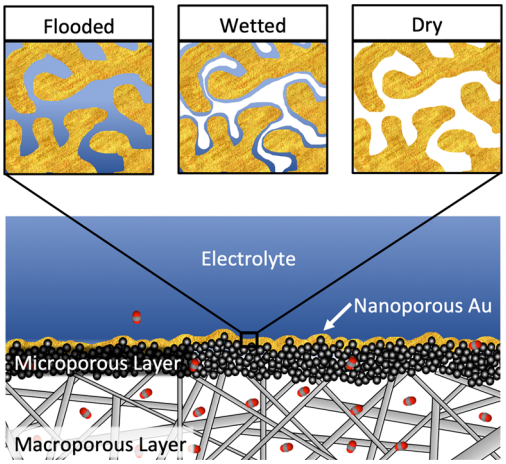

Figure 1. Schematic of the nanoporous gold (np-Au) gas diffusion electrode. The bottom image shows the electrode structure. The support consists of carbon fibers in the macroporous layer, on top of which are coated carbon black and PTFE, which make up the microporous layer. The np-Au catalyst layer is coated on top of this. The top three panels show the different configurations that occur in the np-Au catalyst layer during operation: flooded, wetted, and dry.

the diffusion length and substantially increases the CO_2 transport rate to the catalyst surface, enabling higher current densities in the range of 100−1000 mA/cm^2 in state-of-the-art devices.[26,27,30,31] We will refer to this GDE state as wetted. It is also important to note that portions of the catalyst layer in a GDE could potentially be dried out due to inlet gas pressure and evaporative water loss, thus rendering that portion of the catalyst electrochemically inactive, as illustrated in Figure 1. We note that the wetted GDE state is a highly idealized depiction for the sake of discussion and that an actual GDE likely exists as a combination of wetted, flooded, and dried states. Preliminary computational work has been carried out to yield a nascent understanding of the complex interaction between the catalyst and the electrolyte;[21,25,32] while intriguing, there is currently a lack of detailed experimental work to further support an understanding of this triple-phase boundary layer and how it evolves during GDE operation. Here we seek to understand the relationship between electrochemical reduction and catalyst wetting for a nanoporous Au catalyst morphology.

It has previously been demonstrated that nanoporous gold (np-Au) is a promising catalyst for the electrochemical conversion of CO_2 to CO.[7] In an aqueous-based electrochemical CO_2R cell, np-Au has shown improved catalytic selectivity and activity relative to planar Au (pl-Au) due to the high density of under-coordinated active sites,[33] prevalence of grain boundaries,[33,34] and high surface area.[35,36] Furthermore, pH gradients are built up within the nanoporous structure during operation, which leads to locally increased pH conditions that suppress the parasitic hydrogen evolution reaction (HER);[37] however, these prior experiments were only demonstrated in a bulk aqueous electrolyte-based electrochemical CO_2R cell. In this study, np-Au GDEs were used as a model catalyst system for a vapor-fed CO_2R device. We demonstrate that np-Au GDEs achieve >95% selectivity for CO at partial current densities for CO production (J_{CO}) greater than 150 mA/cm^2. An outstanding question for researchers is what portion of the GDE catalyst layer meaningfully contributes to active catalysis. We employed scanning electron microscopy (SEM), copper underpotential deposition (Cu UPD), secondary ion mass spectroscopy (SIMS), and electrochemical analysis to determine the fraction of the nanoporous GDE catalyst that is flooded/wetted and dry during operation. Through this combination of experiments, we found that only 56% of the available catalyst is active under operating conditions and that the bottom 75% of the catalyst layer exhibits the largest difference in wetting relative to an aqueous CO_2-fed system. These investigations demonstrate an improved method for *in situ* catalyst characterization in GDE devices, and they contribute to understanding the factors that optimize catalytic performance.

The np-Au GDEs were fabricated by co-deposition of Au/Ag alloy films from Au and Ag sources by electron beam evaporation onto the microporous side of a carbon paper substrate (Sigracet 38BC) to produce a Au_xAg_{1-x} alloy of uniform distribution. The atomic percent of Au relative to Ag was tuned by varying the deposition rates of each metal. The np-Au electrode was produced by etching the Au_xAg_{1-x} alloy in concentrated nitric acid (70% weight/volume) for 15 min at room temperature. Concentrated nitric acid selectively dissolves the Ag from the Au_xAg_{1-x} alloy to yield the desired np-Au morphology. The etched electrodes were then thoroughly rinsed with water, dried under a stream of nitrogen and then overnight in vacuo to yield the np-Au electrode. Residual Ag in the etched electrodes was determined by SIMS to be 1.3%. This value is in line with expected residual Ag values from the literature.[7,38] See the experimental methods in the Supporting Information for more details and Figure S1 for SEM images of the fabrication process.

Representative, top-down SEM images for a range of 300 nm thick np-Au samples of varying gold atomic percent ($\%_{Au}$) from 15%$_{Au}$ to 35%$_{Au}$ and a 100%$_{Au}$ pl-Au control are shown in Figure 2a−d and Figure S2. Clear morphological distinctions can be observed between the samples of different Au fractions. The electrode morphologies consist of a three-dimensional network of interconnected Au ligaments and pores separated by cracks that leave open space in the np-Au film. These cracks in the np-Au morphology are due to volume contractions (10−30%) that occur within the film during the removal of Ag from the alloy.[38] The crack width and length notably increased below 25%$_{Au}$ and resulted in a discontinuous film at 15%$_{Au}$, through which the underlying carbon paper substrate is visible (Figure S2a−c). The size of the cracks at 35%$_{Au}$ is greatly diminished as a near-continuous network of ligaments was eventually achieved (Figure S2g−i). However, the uneven nature of the underlying carbon paper substrate makes this visualization difficult. To better understand the morphological changes, np-Au was deposited on planar Si substrates as shown in Figure S3. A nanoporous morphology is no longer observed above 45%$_{Au}$ due to the lack of continuous channels of Ag present in the base alloy (Figure S2j−l). At these Au/Ag ratios, Au forms a protective barrier that prevents nitric acid from

https://doi.org/10.1021/acsenergylett.1c02267
ACS Energy Lett. 2022, 7, 871−879

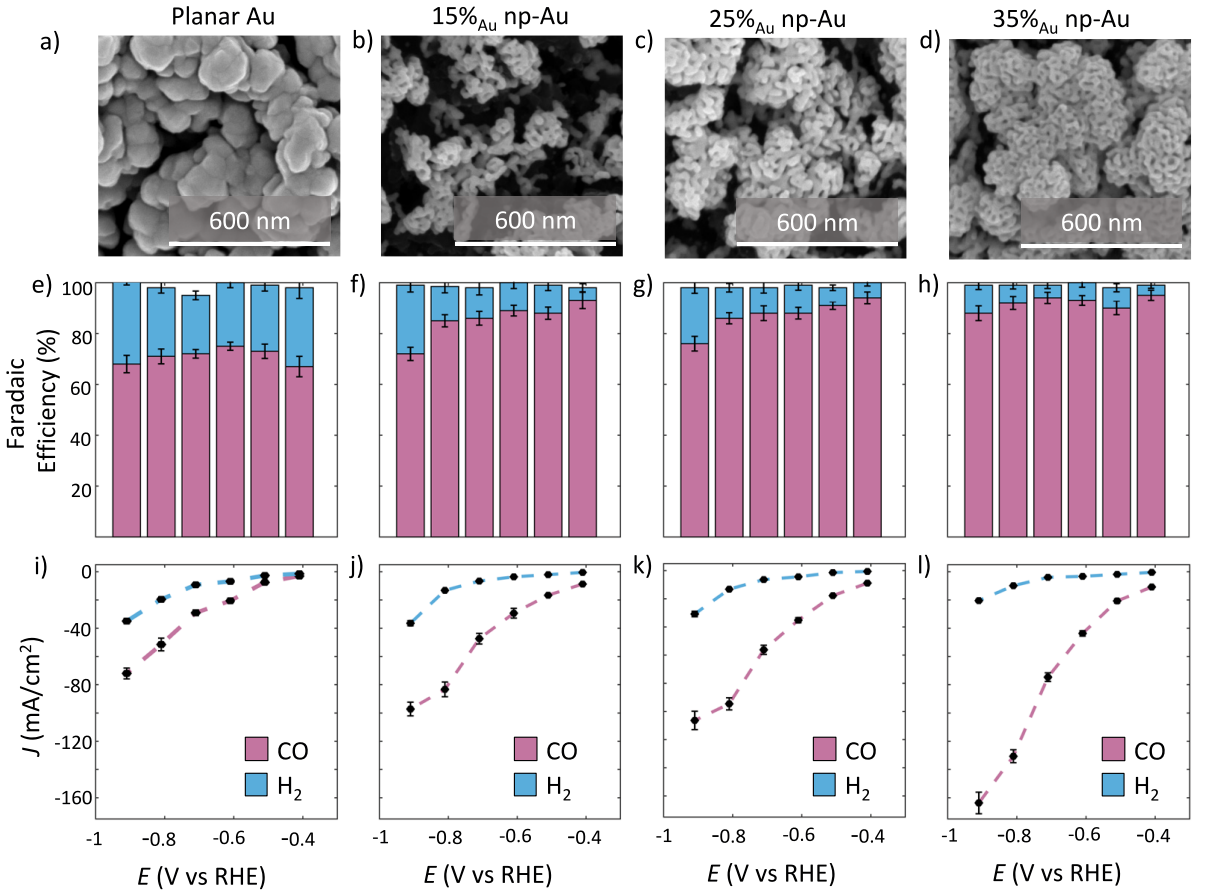

Figure 2. SEM characterization of planar gold (pl-Au) and nanoporous gold (np-Au) electrodes with varying gold atomic percent ($\%_{Au}$) (a–d). CO_2R performance of the pl-Au and np-Au electrodes is shown via Faradaic efficiencies (e–h) and partial current densities (i–l). For all plots, CO is denoted in pink and H_2 in blue. Each data point is the average of three distinct electrodes.

penetrating deeper into the alloy to remove residual Ag.[38] The coarseness of the nanoporous ligaments and pores is modestly reduced as the $\%_{Au}$ is increased. Cross-sectional SEM demonstrates that the nanoporous ligaments are consistently distributed throughout the entire volume of the film after de-alloying (Figure S4). Figure S1 shows SEM images of the bare carbon paper substrate, the Au_xAg_{1-x} base alloy before the nitric acid etch, and the de-alloyed substrate after the nitric acid etch.

CO_2R performance for each electrode was evaluated in a two-compartment flow cell (see experimental methods in the Supporting Information). A Selemion anion exchange membrane was used to separate the Pt mesh counter electrode from the np-Au working electrode. A 1 M $KHCO_3$ electrolyte saturated with CO_2 was independently recirculated through the anode and cathode chambers at a flow rate of 15 mL/min. Despite the fact that the increased alkalinity of KOH electrolytes has been shown to improve CO_2R selectivity,[28,29,39] KOH is considered to be a sacrificial medium because the hydroxide anions react with the CO_2 to form bicarbonate and carbonate.[40] The carbonate salts are then known to precipitate out of solution and potentially clog the pores of the anion exchange membrane,[41] which necessitates that the KOH electrolyte be continuously replenished throughout CO_2R experiments.[42,43] Additionally, carbonate formation at high pH and subsequent reoxidation to CO_2 at the anode reduces the overall energy efficiency of CO_2R devices.[44] $KHCO_3$ was selected as our electrolyte, as recent studies have shown that it can achieve CO_2R performance comparable to that of KOH without the need to replenish the electrolyte.[7,28,45] However, it should be noted that $KHCO_3$ is likely susceptible to carbonate formation due to the high pH values that likely occur at the catalyst layer.[46] The CO_2 gas was delivered through a serpentine channel located behind the GDE at a constant flow rate of 50 standard cubic centimeters per minute (SCCM) unless otherwise noted. A leakless Ag/AgCl electrode was used as the reference electrode. A gas chromatograph was used to quantify the concentration of product gases in the effluent stream, and a potentiostat was used to control the applied electrochemical potential. All electrode potentials (E) are reported relative to the reversible hydrogen electrode (RHE) scale (V_{RHE}). Carbon paper controls were carried out to rule out possible CO_2R product formation due to the base substrate and supporting electrolyte (see SI for further details).

Figure 2e–h shows the FE values of pl-Au and np-Au GDEs (300 nm thick) for both CO and H_2, with the corresponding partial current densities shown in Figure 2i–l, as a function of applied potential between the range from −0.42 to −0.92 V_{RHE} in a CO_2 vapor-fed configuration. Each measurement represents the average value obtained from three distinct electrodes, and the error bars denote one standard deviation above the mean. From these data, we see that the pl-Au GDE exhibits a maximum current density (J) of 106 mA/cm^2 at −0.92 V_{RHE} and a maximum FE for CO of 82% at −0.82 V_{RHE}. After benchmarking the performance of the pl-Au electrode as

https://doi.org/10.1021/acsenergylett.1c02267
ACS Energy Lett. 2022, 7, 871−879

a reference, we then tested a series of np-Au electrodes to evaluate the performance over a range of varying $\%_{Au}$. Both $15\%_{Au}$ and $25\%_{Au}$ exhibited similar FEs and partial current densities for CO (J_{CO}), with a modest improvement over the pl-Au. The $35\%_{Au}$ electrode significantly outperforms the pl-Au across the entire potential range, with a minimum twofold enhancement in J_{CO}. The maximum J_{CO} of 164 mA/cm^2 with a FE of 88% for CO was attained at −0.92 V_{RHE}. The FE for CO remains above 90% at even lower applied potentials, with a peak FE for CO of 95% observed at −0.42 V_{RHE}. Additionally, the J_{CO} of the $35\%_{Au}$ electrodes at −0.82 V_{RHE} is higher, at 130 mA/cm^2, than those for the −0.92 V_{RHE} data points for all other electrodes. We hypothesize that the enhanced performance of the $35\%_{Au}$ electrode is due to the nearly contiguous ligament coverage across the electrode surface, which may improve electrolyte wetting, decrease the potential for flooding, and increase the residency of CO_2 in the catalyst layer by reducing the distribution of cracks that would otherwise allow the gas to easily circumvent the catalytically active regions. Carbon paper systems are well known to degrade over the course of 1 h, and we confirmed these past reports when assessing the long-term stability of our system during a long chronoamperometry experiment.[28,47] The system was stable for an initial 45 min, and then HER steadily increased as the carbon paper base substrate became increasingly flooded (Figure S9).

We sought to better understand the difference in performance between the np-Au catalysts of varying $\%_{Au}$ by understanding how the electrolyte interacts with each system. Catalyst wetting is a critical component of device performance, and we therefore carried out contact angle analyses of each of the electrodes to understand the connection between the np-Au structure and the macroscopic wetting properties of the device. Figure S6 shows the contact angles of a variety of samples, including the base carbon paper, 300 nm thick Au-on-Si substrate, pl-Au on carbon paper, and np-Au on carbon paper. The carbon paper itself is hydrophobic, as it contains a fluorinated microporous layer and exhibits a contact angle of 159°, whereas the 300 nm thick pl-Au GDE resulted in a contact angle of 106°. The $15\%_{Au}$ GDE sample had a hydrophobicity similar to that of the pl-Au reference, with a contact angle of 108°. Interestingly, the $35\%_{Au}$ was found to be the most hydrophilic, with a contact angle of 59°. We attribute the higher hydrophobicity of lower $\%_{Au}$ samples to the large cracks in the catalyst layer that penetrate through to the hydrophobic substrate, which allows the water droplet to come into contact with the fluorinated microporous layer. The improved metal coverage in the $35\%_{Au}$ sample minimized contact with the microporous layer. Therefore, the hydrophilic network of pores is able to wick water into its structure and lower the contact angle. While this provides correlation between wetting and device performance, this does not explain the improvement in CO_2R performance, as catalyst hydrophobicity has been demonstrated to improve CO_2R.[48−51] To better understand our system, we must consider wetting at the surface of the electrolyte−catalyst interface as distinct from the bulk properties highlighted by contact angle analysis.

The surface area of a catalyst is traditionally quantified by double-layer capacitance electrochemically active surface area (ECSA) measurements,[52,53] Brunauer−Emmett−Teller (BET) measurements,[54,55] and Cu UPD.[7,56] ECSA measurements effectively determine the total surface area in contact with the electrolyte, BET measurements effectively determine the total dry surface area, and Cu UPD determines the specific surface area of the Au catalyst as the Cu selectively deposits on the Au metal only. Cu UPD allows us to determine the surface area of the catalyst and probe the wetting of the catalyst surface by evaluating where the liquid electrolyte is present and absent. The Cu UPD process electroplates a monolayer of Cu onto Au surfaces exposed to the electrolyte.[7] It is then possible to integrate the area of the anodic peak obtained from Cu stripping in the cyclic voltammogram to determine how much Cu was deposited on the Au surface, since the charge passed during the experiment is proportional to the surface area of the Au catalyst.[7,56,57] From this measurement, we are able to determine the surface area of the catalyst that is in contact with the electrolyte (see Supporting Information for experimental details). We first measured the surface area of 300 nm of pl-Au deposited onto a flat silicon wafer (pl-Au on Si) as a baseline and normalized all subsequent Cu UPD measurements to this value (Figure 3a). A pl-Au electrode on carbon paper with 300 nm of Au deposited on it exhibited a 15× area enhancement compared to the pl-Au on silicon. This area enhancement indicated that the irregular carbon paper base substrate increases the rugosity and subsequently the surface area of the pl-Au electrode. In comparison, a $35\%_{Au}$ np-Au electrode on carbon paper etched from a 300 nm thick Au/Ag alloy resulted in a 78× increase of surface area compared to the pl-Au on Si and a 5× increase of surface area compared to the pl-Au electrode on carbon paper. This significant increase in surface area demonstrated that the nanotexturing method greatly enhanced the available surface area of a np-Au electrode

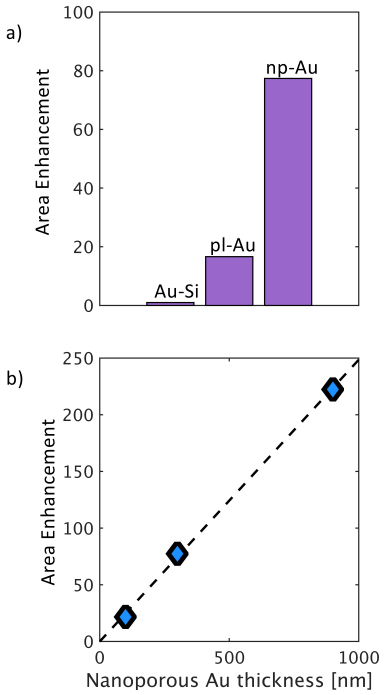

Figure 3. Characterization of np-Au film surface area via comparative Cu underpotential deposition (Cu UPD) surface area measurements. (a) Relative surface area enhancements of a 300 nm thick pl-Au on silicon (Au−Si), a 300 nm thick pl-Au on carbon paper electrode (pl-Au), and a 300 nm thick $35\%_{Au}$ np-Au on carbon paper electrode (np-Au) normalized to the Au−Si sample. (b) Surface area enhancement of 100, 300, and 900 nm thick $35\%_{Au}$ np-Au.

https://doi.org/10.1021/acsenergylett.1c02267
ACS Energy Lett. 2022, 7, 871−879

relative to a pl-Au electrode. While a cross-sectionally isotropic np-Au morphology was observed by SEM (Figure S4), we sought to verify this observation with Cu UPD experiments. To achieve this, three distinct $35\%_{Au}$ electrodes etched from a Au/Ag alloy with thicknesses of 100, 300, and 900 nm were fabricated and intentionally flooded by soaking them in an aqueous CO_2-fed electrochemical cell to ensure that the entire surface area of the catalyst layer was electrochemically accessible (Figure 3b). We found that the surface area as measured by Cu UPD increased linearly with the thickness of the catalyst layer. The linear increase in surface area with film thickness confirmed that our electrodes are indeed cross-sectionally isotropic and that the Cu^{2+} ions in solution penetrated into the entire depth of the catalyst layer in the aqueous CO_2-fed configuration. If the entire np-Au film was not accessible to the electrolyte, we would have observed that the surface area enhancement would taper off with increasing np-Au film thickness since some of the Cu^{2+} ions would be unable to diffuse throughout the extent of the np-Au ligament network.

Interestingly, we observed a 5× increase in surface area for the $35\%_{Au}$ sample compared to the pl-Au, but only a 2−3.5× increase in current density (J) during electrochemical CO_2R. To understand the discrepancy between surface area and J, we carried out a set of Cu UPD experiments under CO_2 vapor-fed conditions. We note that N_2 was used instead of CO_2 to simulate the GDE conditions since CO_2 was found to interact with the Cu UPD electrolyte solution (Figure 4a). We expect that the surface area calculated by Cu UPD from an electrode in an aqueous CO_2-fed system represents a more accurate surface area of the np-Au catalyst layer, as the entirety of the Au is in contact with the electrolyte, i.e., fully flooded. The surface area of a fully flooded np-Au electrode was then normalized to 1, and any deviation from this value by a CO_2-vapor-fed electrode can be attributed to a percentage of the catalyst layer being inaccessible to the electrolyte as a result of the gas flow. At a flow rate of 50 SCCM, the measured surface area of a $35\%_{Au}$ electrode decreased to 56% of its flooded value, indicating that only a portion of the electrode is accessible to the electrolyte. As the flow rate was reduced to 10 SCCM and then 2 SCCM, the accessible surface area increased to 66% and then 87% of the total available surface area, respectively. We attribute this observation to an increase of flooded pores in the entire GDE (including the underlying carbon paper substrate) due to the reduced pressure within the porous network as a result of the reduced gas flow rate. To evaluate this interpretation, we performed a series of CO_2R experiments on 300 nm thick, $35\%_{Au}$ np-Au electrodes at 50, 10, and 2 SCCM at an applied potential of −0.92 V_{RHE}. We found that the current density decreased from 190 mA/cm^2 at a flow rate of 50 SCCM to 107 mA/cm^2 at 10 SCCM and further to 91 mA/cm^2 at the lowest flow rate of 2 SCCM (Figure 4c). This decrease in current density indicates that the entire GDE becomes increasingly flooded as the flow rate of CO_2 is reduced and the pores in the carbon paper substrate itself become increasingly flooded. To further validate this interpretation, we monitored the FE for H_2 of each electrode and found it increased from 12% up to 48% as the flow rate was reduced from 50 to 2 SCCM (Figure 4b). The increased H_2 production with reduced CO_2 flow rate indicates that the catalyst layer cannot effectively perform CO_2R and instead engages in parasitic HER in the increasingly flooded pores. These results agree with previously reported literature which

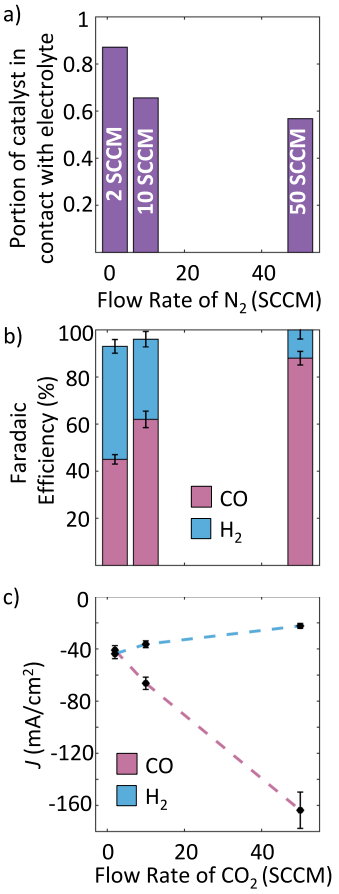

Figure 4. Characterization of the catalytically active np-Au surface area as a function of gas flow rate and its impact on CO_2R. (a) Relative surface area of three identical 300 nm thick, vapor-fed, $35\%_{Au}$ np-Au electrodes under different N_2 flow rates normalized to the surface area of the same electrode in an aqueous-fed system. (b) Faradaic efficiencies of the electrodes at different CO_2 flow rates. (c) Partial current densities of the electrodes at different CO_2 flow rates. All experiments for (b) and (c) were carried out at an applied potential of −0.92 V_{RHE}.

has indicated an optimally wetted state that is highly selective for CO_2R.[21,26,32] In our system, this optimal state is highly impacted by flow rate. At high flow rates we hypothesize that a build up in pressure improves transport through the GDE and staves off flooding. At low flow rates the electrolyte floods the entire GDE, resulting in mass transport limitations and increased HER. It is unlikely that this flooding is occurring in the catalyst layer alone, as previous literature has demonstrated that the CO_2 diffusion layer thickness is on the order of microns rather than nanometers.[58−60] We present in Figure 1 the three idealized states in which a catalyst layer can exist. In reality it is likely that the true wetting of the catalyst layer occurs as a combination of all three idealized states.

In order to verify that these Cu UPD results correspond to the fraction of the wetted catalyst, we electroplated Cu onto a fully flooded GDE and compared it to that of an *in situ* electrode during simulated CO_2R conditions (see Supporting Information for more details). This approach should yield an electrode with Cu metal plated onto the regions that were in contact with electrolyte and an absence of Cu where the electrode is dry. Therefore, the presence of Cu serves as a

https://doi.org/10.1021/acsenergylett.1c02267
ACS Energy Lett. 2022, 7, 871−879

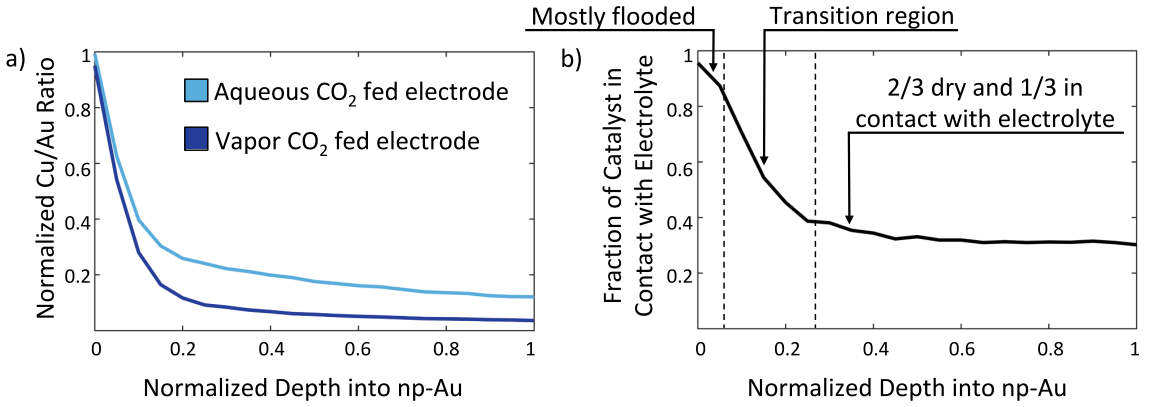

Figure 5. Secondary ion mass spectrometry (SIMS) analysis of np-Au. (a) Normalized Cu counts relative to normalized depth into the np-Au electrode, with 0 as the surface of the np-Au film in contact with the electrolyte and 1 as the bottom of the np-Au film in contact with the microporous layer support. (b) Ratio of the vapor-fed counts to the aqueous-fed counts in (a). This fraction represents the portion of the catalyst that is in contact with the electrolyte as a function of depth within the np-Au film. The vapor-fed system is run at an N_2 flow rate of 50 SCCM.

proxy for wetting within the np-Au. The spatial distribution of Cu within the np-Au electrodes was determined via secondary ion mass spectrometry (SIMS) analysis that was carried out on both an aqueous-fed electrode and a vapor-fed electrode (Figure 5a and Figure S7, respectively). A 300 nm thick pl-Au sample on a flat Si substrate was used as a control sample to determine the ablation time required by SIMS. We found that it took roughly 400 s to ablate through the entire Au layer, as observed by a total reduction of the Au counts and a sharp increase in the Si counts, indicating that the underlying substrate had been reached (Figure S8). These conditions were then applied to the two samples of interest, and we assumed the np-Au electrodes of each sample are nearly identical. Comparing the Cu/Au ratio of each distinct electrode, we found that the total number of integrated Cu/Au counts of the vapor-fed electrode was 57% that of the aqueous-fed electrode (Figure 5a). This SIMS result is in close agreement with our Cu UPD finding that the vapor-fed electrode has 56% the surface area of the aqueous-fed device. Next, we took the ratio of these results to determine the percentage of the vapor-fed electrode that is in contact with the electrolyte as a function of depth (Figure 5b). We define 0 as the surface of the np-Au electrode in contact with the electrolyte and 1 as the bottom np-Au electrode in contact with the microporous layer. If the vapor-fed/aqueous-fed ratio is equal to 1, then the wetting of the two electrodes is equivalent, whereas fractional deviations from 1 indicate that the aqueous-fed electrode has more np-Au in contact with the electrolyte. From this analysis, we found that the vapor/aqueous-fed depth profile can be separated into three distinct regions (Figure 5b). In region 1 (the top 10% of the catalyst), both electrodes have a comparable wetting, which indicates that the vapor-fed electrode is predominantly flooded in this region. Region 2 is a transition zone where the wetting in the catalyst layer of the vapor-fed electrode is increasingly reduced with increasing depth as compared to the aqueous-fed electrode. Region 3 consists of the bottom 75% of the catalyst layer, and here the vapor-fed electrode has approximately two-thirds less wetting than the aqueous-fed electrode. This finding shows that a significant fraction of the catalyst layer of the vapor-fed electrode is not in contact with the bulk electrolyte and therefore cannot contribute to CO_2R. These techniques allow us to determine the percentage of the active catalyst that actually participates in CO_2R. We anticipate that these previously unknown results will allow for improved GDE designs that are capable of harnessing more of the available electrode surface area to drive electrocatalytic CO_2R at high current densities while maintaining appropriate reaction selectivity.

In conclusion, we have provided a new method for evaluating the catalytically active region fraction in gas diffusion electrodes for carbon dioxide reduction. Through a combination of Cu underpotential deposition measurements and secondary ion mass spectrometry depth profile analyses, we were able to show that the top 10% of the np-Au layer of a CO_2 vapor-fed GDE is flooded, while the rest of the catalyst layer exists as a combination of flooded/wetted and nearly completely dry states. Strikingly, 43% of the np-Au catalyst is not in contact with the bulk electrolyte at all during operation. In addition to providing a new approach for elucidating the catalytically active regions of CO_2 vapor-fed devices, we also demonstrate a highly active np-Au GDE for CO_2R that attained a FE for CO of up to 95% and a J_{CO} of 168 mA/cm^2. We hope that the new insights presented herein will enable an improved understanding of the factors that govern catalytic activity in CO_2 vapor-fed GDEs and will allow for maximizing the amount of catalyst that contributes toward CO_2R.

■ ASSOCIATED CONTENT

Supporting Information

The Supporting Information is available free of charge at https://pubs.acs.org/doi/10.1021/acsenergylett.1c02267.

Description of the materials and fabrication process for nanoporous gold electrodes, scanning electron micrographs, description of the electrochemical carbon dioxide reduction experimental setup, contact angle measurement data, Cu UPD measurements, SIMS measurements, and long-term chronoamperometry data, including Figures S1−S9 (PDF)

■ AUTHOR INFORMATION

Corresponding Author

Harry A. Atwater − *Liquid Sunlight Alliance and Department of Applied Physics and Material Science, California Institute of Technology, Pasadena, California 91125, United States;*

https://doi.org/10.1021/acsenergylett.1c02267
ACS Energy Lett. 2022, 7, 871−879

orcid.org/0000-0001-9435-0201; Email: haa@caltech.edu

Authors

Aidan Q. Fenwick − *Department of Chemistry, California Institute of Technology, Pasadena, California 91125, United States; Liquid Sunlight Alliance, California Institute of Technology, Pasadena, California 91125, United States*

Alex J. Welch − *Liquid Sunlight Alliance and Department of Applied Physics and Material Science, California Institute of Technology, Pasadena, California 91125, United States;* orcid.org/0000-0003-2132-9617

Xueqian Li − *Liquid Sunlight Alliance and Department of Applied Physics and Material Science, California Institute of Technology, Pasadena, California 91125, United States*

Ian Sullivan − *Department of Chemistry, California Institute of Technology, Pasadena, California 91125, United States; Department of Applied Physics and Material Science, California Institute of Technology, Pasadena, California 91125, United States;* orcid.org/0000-0003-0632-4607

Joseph S. DuChene − *Department of Chemistry, University of Massachusetts, Amherst, Massachusetts 01003, United States;* orcid.org/0000-0002-7145-323X

Chengxiang Xiang − *Department of Chemistry, California Institute of Technology, Pasadena, California 91125, United States; Department of Applied Physics and Material Science, California Institute of Technology, Pasadena, California 91125, United States;* orcid.org/0000-0002-1698-6754

Complete contact information is available at: https://pubs.acs.org/10.1021/acsenergylett.1c02267

Author Contributions

†A.Q.F. and A.J.W. contributed equally to this work.

Notes

Any opinions, findings, and conclusions expressed in this material are those of the authors and do not necessarily reflect those of DOE or NSF.

The authors declare no competing financial interest.

■ ACKNOWLEDGMENTS

This work was performed within the Liquid Sunlight Alliance, which is supported by the U.S. Department of Energy, Office of Science, Office of Basic Energy Sciences, Fuels from Sunlight Hub under Award Number DE-SC0021266. A.J.W. acknowledges support from the Resnick Sustainability Institute at Caltech for fellowship support and from the National Science Foundation (NSF) Graduate Research Fellowship Program under Base Award No. 174530.

■ REFERENCES

(1) Garg, S.; Li, M.; Weber, A. Z.; Ge, L.; Li, L.; Rudolph, V.; Wang, G.; Rufford, T. E. Advances and Challenges in Electrochemical CO_2 Reduction Processes: An Engineering and Design Perspective Looking beyond New Catalyst Materials. *J. Mater. Chem. A* **2020**, *8* (4), 1511−1544.

(2) Schreier, M.; Héroguel, F.; Steier, L.; Ahmad, S.; Luterbacher, J. S.; Mayer, M. T.; Luo, J.; Grätzel, M. Solar Conversion of Co2 to CO Using Earth-Abundant Electrocatalysts Prepared by Atomic Layer Modification of CuO. *Nat. Energy* **2017**, *2* (7), 17087.

(3) Lin, S.; Diercks, C. S.; Zhang, Y. B.; Kornienko, N.; Nichols, E. M.; Zhao, Y.; Paris, A. R.; Kim, D.; Yang, P.; Yaghi, O. M.; Chang, C. J. Covalent Organic Frameworks Comprising Cobalt Porphyrins for Catalytic CO_2 Reduction in Water. *Science* **2015**, *349* (6253), 1208−1213.

(4) Kuhl, K. P.; Cave, E. R.; Abram, D. N.; Jaramillo, T. F. New Insights into the Electrochemical Reduction of Carbon Dioxide on Metallic Copper Surfaces. *Energy Environ. Sci.* **2012**, *5* (5), 7050−7059.

(5) Kuhl, K. P.; Hatsukade, T.; Cave, E. R.; Abram, D. N.; Kibsgaard, J.; Jaramillo, T. F. Electrocatalytic Conversion of Carbon Dioxide to Methane and Methanol on Transition Metal Surfaces. *J. Am. Chem. Soc.* **2014**, *136* (40), 14107−14113.

(6) Hatsukade, T.; Kuhl, K. P.; Cave, E. R.; Abram, D. N.; Jaramillo, T. F. Insights into the Electrocatalytic Reduction of CO_2 on Metallic Silver Surfaces. *Phys. Chem. Chem. Phys.* **2014**, *16* (27), 13814−13819.

(7) Welch, A. J.; Duchene, J. S.; Tagliabue, G.; Davoyan, A.; Cheng, W. H.; Atwater, H. A. Nanoporous Gold as a Highly Selective and Active Carbon Dioxide Reduction Catalyst. *ACS Appl. Energy Mater.* **2019**, *2* (1), 164−170.

(8) Rosen, B. A.; Salehi-Khojin, A.; Thorson, M. R.; Zhu, W.; Whipple, D. T.; Kenis, P. J. A.; Masel, R. I. Ionic Liquid − Mediated Selective. *Science* **2011**, *334* (6056), 643−644.

(9) Yang, J.; Ma, W.; Chen, D.; Holmen, A.; Davis, B. H. Fischer−Tropsch Synthesis: A Review of the Effect of CO Conversion on Methane Selectivity. *Appl. Catal. A Gen.* **2014**, *470*, 250−260.

(10) Verma, S.; Kim, B.; Jhong, H. R. M.; Ma, S.; Kenis, P. J. A. A Gross-Margin Model for Defining Technoeconomic Benchmarks in the Electroreduction of CO_2. *ChemSusChem* **2016**, *9* (15), 1972−1979.

(11) Hernández, S.; Farkhondehfal, M. A.; Sastre, F.; Makkee, M.; Saracco, G.; Russo, N. Syngas Production from Electrochemical Reduction of CO_2: Current Status and Prospective Implementation. *Green Chem.* **2017**, *19* (10), 2326−2346.

(12) Pruett, R. L.; Smith, J. A. A Low-Pressure System for Producing Normal Aldehydes by Hydroformylation of α Olefins. *J. Org. Chem.* **1969**, *34* (2), 327−330.

(13) Jhong, H. R. M.; Ma, S.; Kenis, P. J. Electrochemical Conversion of CO_2 to Useful Chemicals: Current Status, Remaining Challenges, and Future Opportunities. *Curr. Opin. Chem. Eng.* **2013**, *2* (2), 191−199.

(14) Bloemacher, D. Carbonyl Iron Powders: Its Production and New Developments. *Met. Powder Rep.* **1990**, *45* (2), 117−119.

(15) Bushuyev, O. S.; De Luna, P.; Dinh, C. T.; Tao, L.; Saur, G.; van de Lagemaat, J.; Kelley, S. O.; Sargent, E. H. What Should We Make with CO_2 and How Can We Make It? *Joule* **2018**, *2* (5), 825−832.

(16) Nitopi, S.; Bertheussen, E.; Scott, S. B.; Liu, X.; Engstfeld, A. K.; Horch, S.; Seger, B.; Stephens, I. E. L.; Chan, K.; Hahn, C.; Nørskov, J. K.; Jaramillo, T. F.; Chorkendorff, I. Progress and Perspectives of Electrochemical CO_2 Reduction on Copper in Aqueous Electrolyte. *Chem. Rev.* **2019**, *119* (12), 7610−7672.

(17) Lu, Q.; Rosen, J.; Zhou, Y.; Hutchings, G. S.; Kimmel, Y. C.; Chen, J. G.; Jiao, F. A Selective and Efficient Electrocatalyst for Carbon Dioxide Reduction. *Nat. Commun.* **2014**, *5*, 1−6.

(18) Asadi, M.; Kim, K.; Liu, C.; Addepalli, A. V.; Abbasi, P.; Yasaei, P.; Phillips, P.; Behranginia, A.; Cerrato, J. M.; Haasch, R.; Zapol, P.; Kumar, B.; Klie, R. F.; Abiade, J.; Curtiss, L. A.; Salehi-Khojin, A. Nanostructured Transition Metal Dichalcogenide Electrocatalysts for CO_2 Reduction in Ionic Liquid. *Science* **2016**, *353* (6298), 467−470.

(19) Gao, D.; Zhou, H.; Wang, J.; Miao, S.; Yang, F.; Wang, G.; Wang, J.; Bao, X. Size-Dependent Electrocatalytic Reduction of CO_2 over Pd Nanoparticles. *J. Am. Chem. Soc.* **2015**, *137* (13), 4288−4291.

(20) Chen, Y.; Li, C. W.; Kanan, M. W. Aqueous CO_2 Reduction at Very Low Overpotential on Oxide-Derived Au Nanoparticles. *J. Am. Chem. Soc.* **2012**, *134* (49), 19969−19972.

(21) Weng, L. C.; Bell, A. T.; Weber, A. Z. Modeling Gas-Diffusion Electrodes for CO_2 Reduction. *Phys. Chem. Chem. Phys.* **2018**, *20* (25), 16973−16984.

(22) Ma, M.; Clark, E. L.; Therkildsen, K. T.; Dalsgaard, S.; Chorkendorff, I.; Seger, B. Insights into the Carbon Balance for CO_2 Electroreduction on Cu Using Gas Diffusion Electrode Reactor Designs. *Energy Environ. Sci.* **2020**, *13* (3), 977−985.

(23) Singh, M. R.; Goodpaster, J. D.; Weber, A. Z.; Head-Gordon, M.; Bell, A. T. Mechanistic Insights into Electrochemical Reduction of CO_2 over Ag Using Density Functional Theory and Transport Models. *Proc. Natl. Acad. Sci. U. S. A.* **2017**, *114* (42), E8812−E8821.
(24) Weekes, D. M.; Salvatore, D. A.; Reyes, A.; Huang, A.; Berlinguette, C. P. Electrolytic CO_2 Reduction in a Flow Cell. *Acc. Chem. Res.* **2018**, *51* (4), 910−918.
(25) Higgins, D.; Hahn, C.; Xiang, C.; Jaramillo, T. F.; Weber, A. Z. Gas-Diffusion Electrodes for Carbon Dioxide Reduction: A New Paradigm. *ACS Energy Lett.* **2019**, *4* (1), 317−324.
(26) García de Arquer, F. P.; Dinh, C. T.; Ozden, A.; Wicks, J.; McCallum, C.; Kirmani, A. R.; Nam, D. H.; Gabardo, C.; Seifitokaldani, A.; Wang, X.; Li, Y. C.; Li, F.; Edwards, J.; Richter, L. J.; Thorpe, S. J.; Sinton, D.; Sargent, E. H. CO_2 Electrolysis to Multicarbon Products at Activities Greater than 1 A Cm-2. *Science* **2020**, *367* (6478), 661−666.
(27) Grigioni, I.; Sagar, L. K.; Li, Y. C.; Lee, G.; Yan, Y.; Bertens, K.; Miao, R. K.; Wang, X.; Abed, J.; Won, D. H.; Garciá De Arquer, F. P.; Ip, A. H.; Sinton, D.; Sargent, E. H. CO_2 Electroreduction to Formate at a Partial Current Density of 930 MA Cm-2with InP Colloidal Quantum Dot Derived Catalysts. *ACS Energy Lett.* **2021**, *6* (1), 79−84.
(28) Dinh, C. T.; García De Arquer, F. P.; Sinton, D.; Sargent, E. H. High Rate, Selective, and Stable Electroreduction of Co2 to Co in Basic and Neutral Media. *ACS Energy Lett.* **2018**, *3* (11), 2835−2840.
(29) Verma, S.; Hamasaki, Y.; Kim, C.; Huang, W.; Lu, S.; Jhong, H. R. M.; Gewirth, A. A.; Fujigaya, T.; Nakashima, N.; Kenis, P. J. A. Insights into the Low Overpotential Electroreduction of CO_2 to CO on a Supported Gold Catalyst in an Alkaline Flow Electrolyzer. *ACS Energy Lett.* **2018**, *3* (1), 193−198.
(30) Nam, D. H.; De Luna, P.; Rosas-Hernández, A.; Thevenon, A.; Li, F.; Agapie, T.; Peters, J. C.; Shekhah, O.; Eddaoudi, M.; Sargent, E. H. Molecular Enhancement of Heterogeneous CO_2 Reduction. *Nat. Mater.* **2020**, *19* (3), 266−276.
(31) Li, F.; Thevenon, A.; Rosas-Hernández, A.; Wang, Z.; Li, Y.; Gabardo, C. M.; Ozden, A.; Dinh, C. T.; Li, J.; Wang, Y.; Edwards, J. P.; Xu, Y.; McCallum, C.; Tao, L.; Liang, Z. Q.; Luo, M.; Wang, X.; Li, H.; O'Brien, C. P.; Tan, C. S.; Nam, D. H.; Quintero-Bermudez, R.; Zhuang, T. T.; Li, Y. C.; Han, Z.; Britt, R. D.; Sinton, D.; Agapie, T.; Peters, J. C.; Sargent, E. H. Molecular Tuning of CO_2-to-Ethylene Conversion. *Nature* **2020**, *577* (7791), 509−513.
(32) Nesbitt, N. T.; Burdyny, T.; Simonson, H.; Salvatore, D.; Bohra, D.; Kas, R.; Smith, W. A. Liquid-Solid Boundaries Dominate Activity of CO_2Reduction on Gas-Diffusion Electrodes. *ACS Catal.* **2020**, *10* (23), 14093−14106.
(33) Zhang, W.; He, J.; Liu, S.; Niu, W.; Liu, P.; Zhao, Y.; Pang, F.; Xi, W.; Chen, M.; Zhang, W.; Pang, S.-S.; Ding, Y. Atomic Origins of High Electrochemical CO_2 Reduction Efficiency on Nanoporous Gold. *Nanoscale* **2018**, *10* (18), 8372−8376.
(34) Chen, C.; Zhang, B.; Zhong, J.; Cheng, Z. Selective Electrochemical CO_2 Reduction over Highly Porous Gold Films. *J. Mater. Chem. A* **2017**, *5* (41), 21955−21964.
(35) Wang, R.; Wang, C.; Cai, W.-B.; Ding, Y. Ultralow-Platinum-Loading High-Performance Nanoporous Electrocatalysts with Nano-engineered Surface Structures. *Adv. Mater.* **2010**, *22* (16), 1845−1848.
(36) Sukeri, A.; Saravia, L. P. H.; Bertotti, M. A Facile Electrochemical Approach to Fabricate a Nanoporous Gold Film Electrode and Its Electrocatalytic Activity towards Dissolved Oxygen Reduction. *Phys. Chem. Chem. Phys.* **2015**, *17* (43), 28510−28514.
(37) Hall, A. S.; Yoon, Y.; Wuttig, A.; Surendranath, Y. Mesostructure-Induced Selectivity in CO_2 Reduction Catalysis. *J. Am. Chem. Soc.* **2015**, *137* (47), 14834−14837.
(38) Biener, J.; Biener, M. M.; Madix, R. J.; Friend, C. M. Nanoporous Gold: Understanding the Origin of the Reactivity of a 21st Century Catalyst Made by Pre-Columbian Technology. *ACS Catal.* **2015**, *5* (11), 6263−6270.
(39) Verma, S.; Lu, X.; Ma, S.; Masel, R. I.; Kenis, P. J. A. The Effect of Electrolyte Composition on the Electroreduction of CO_2 to CO on Ag Based Gas Diffusion Electrodes. *Phys. Chem. Chem. Phys.* **2016**, *18* (10), 7075−7084.
(40) Winter, M.; Brodd, R. J. What Are Batteries, Fuel Cells, and Supercapacitors? *Chem. Rev.* **2004**, *104* (10), 4245−4269.
(41) Gülzow, E.; Schulze, M. Long-Term Operation of AFC Electrodes with CO_2 Containing Gases. *J. Power Sources* **2004**, *127* (1−2), 243−251.
(42) Gülzow, E. Alkaline Fuel Cells: A Critical View. *J. Power Sources* **1996**, *61* (1−2), 99−104.
(43) Gouérec, P.; Poletto, L.; Denizot, J.; Sanchez-Cortezon, E.; Miners, J. H. The Evolution of the Performance of Alkaline Fuel Cells with Circulating Electrolyte. *J. Power Sources* **2004**, *129* (2), 193−204.
(44) Rabinowitz, J. A.; Kanan, M. W. The Future of Low-Temperature Carbon Dioxide Electrolysis Depends on Solving One Basic Problem. *Nat. Commun.* **2020**, *11* (1), 10−12.
(45) Möller, T.; Ngo Thanh, T.; Wang, X.; Ju, W.; Jovanov, Z.; Strasser, P. The Product Selectivity Zones in Gas Diffusion Electrodes during the Electrocatalytic Reduction of CO_2. *Energy Environ. Sci.* **2021**, *14* (11), 5995−6006.
(46) Burdyny, T.; Smith, W. A. CO_2 Reduction on Gas-Diffusion Electrodes and Why Catalytic Performance Must Be Assessed at Commercially-Relevant Conditions. *Energy Environ. Sci.* **2019**, *12* (5), 1442−1453.
(47) Dinh, C. T.; Burdyny, T.; Kibria, G.; Seifitokaldani, A.; Gabardo, C. M.; García De Arquer, F. P.; Kiani, A.; Edwards, J. P.; De Luna, P.; Bushuyev, O. S.; Zou, C.; Quintero-Bermudez, R.; Pang, Y.; Sinton, D.; Sargent, E. H. CO_2 Electroreduction to Ethylene via Hydroxide-Mediated Copper Catalysis at an Abrupt Interface. *Science* **2018**, *360* (6390), 783−787.
(48) Kim, B.; Hillman, F.; Ariyoshi, M.; Fujikawa, S.; Kenis, P. J. A. Effects of Composition of the Micro Porous Layer and the Substrate on Performance in the Electrochemical Reduction of CO_2 to CO. *J. Power Sources* **2016**, *312*, 192−198.
(49) Li, M.; Idros, M. N.; Wu, Y.; Burdyny, T.; Garg, S.; Zhao, X. S.; Wang, G.; Rufford, T. E. The Role of Electrode Wettability in Electrochemical Reduction of Carbon Dioxide. *J. Mater. Chem. A* **2021**, *9* (35), 19369−19409.
(50) Wang, G.; Chen, J.; Ding, Y.; Cai, P.; Yi, L.; Li, Y.; Tu, C.; Hou, Y.; Wen, Z.; Dai, L. Electrocatalysis for CO_2conversion: From Fundamentals to Value-Added Products. *Chem. Soc. Rev.* **2021**, *50* (8), 4993−5061.
(51) Wakerley, D.; Lamaison, S.; Ozanam, F.; Menguy, N.; Mercier, D.; Marcus, P.; Fontecave, M.; Mougel, V. Bio-Inspired Hydrophobicity Promotes CO_2 Reduction on a Cu Surface. *Nat. Mater.* **2019**, *18* (11), 1222−1227.
(52) Kas, R.; Yang, K.; Bohra, D.; Kortlever, R.; Burdyny, T.; Smith, W. A. Electrochemical Co2 Reduction on Nanostructured Metal Electrodes: Fact or Defect? *Chem. Sci.* **2020**, *11* (7), 1738−1749.
(53) Cave, E. R.; Montoya, J. H.; Kuhl, K. P.; Abram, D. N.; Hatsukade, T.; Shi, C.; Hahn, C.; Nørskov, J. K.; Jaramillo, T. F. Electrochemical CO_2 Reduction on Au Surfaces: Mechanistic Aspects Regarding the Formation of Major and Minor Products. *Phys. Chem. Chem. Phys.* **2017**, *19* (24), 15856−15863.
(54) Sinha, P.; Datar, A.; Jeong, C.; Deng, X.; Chung, Y. G.; Lin, L. C. Surface Area Determination of Porous Materials Using the Brunauer-Emmett-Teller (BET) Method: Limitations and Improvements. *J. Phys. Chem. C* **2019**, *123* (33), 20195−20209.
(55) Walton, K. S.; Snurr, R. Q. Applicability of the BET Method for Determining Surface Areas of Microporous Metal-Organic Frameworks. *J. Am. Chem. Soc.* **2007**, *129* (27), 8552−8556.
(56) Zhang, B. A.; Ozel, T.; Elias, J. S.; Costentin, C.; Nocera, D. G. Interplay of Homogeneous Reactions, Mass Transport, and Kinetics in Determining Selectivity of the Reduction of CO_2 on Gold Electrodes. *ACS Cent. Sci.* **2019**, *5* (6), 1097−1105.
(57) Ross, M. B.; Dinh, C. T.; Li, Y.; Kim, D.; De Luna, P.; Sargent, E. H.; Yang, P. Tunable Cu Enrichment Enables Designer Syngas Electrosynthesis from CO_2. *J. Am. Chem. Soc.* **2017**, *139* (27), 9359−9363.

https://doi.org/10.1021/acsenergylett.1c02267
ACS Energy Lett. 2022, 7, 871−879

(58) Gupta, N.; Gattrell, M.; MacDougall, B. Calculation for the Cathode Surface Concentrations in the Electrochemical Reduction of CO_2 in KHCO3 Solutions. *J. Appl. Electrochem.* **2006**, *36* (2), 161−172.
(59) Moore, T.; Xia, X.; Baker, S. E.; Duoss, E. B.; Beck, V. A. Elucidating Mass Transport Regimes in Gas Diffusion Electrodes for CO_2Electroreduction. *ACS Energy Lett.* **2021**, *6* (10), 3600−3606.
(60) Lamaison, S.; Wakerley, D.; Kracke, F.; Moore, T.; Zhou, L.; Lee, D. U.; Wang, L.; Hubert, M. A.; Aviles Acosta, J. E.; Gregoire, J. M.; Duoss, E. B.; Baker, S.; Beck, V. A.; Spormann, A. M.; Fontecave, M.; Hahn, C.; Jaramillo, T. F. Designing a Zn−Ag Catalyst Matrix and Electrolyzer System for CO_2 Conversion to CO and Beyond. *Adv. Mater.* **2022**, *34*, 2103963.

https://doi.org/10.1021/acsenergylett.1c02267
ACS Energy Lett. 2022, 7, 871−879